

Carrier-envelope phase on-chip scanner and control of laser beams

Received: 3 April 2023

Accepted: 10 August 2023

Published online: 21 August 2023

 Check for updates

Václav Hanus ¹✉, Beatrix Fehér ¹, Viktória Csajbók ¹, Péter Sándor ¹,
Zsuzsanna Pápa ^{1,2}, Judit Budai², Zilong Wang^{3,4}, Pallabi Paul ^{5,6},
Adriana Szeghalmi ^{5,6} & Péter Dombi ^{1,2}✉

The carrier-envelope phase (CEP) is an important property of few-cycle laser pulses, allowing for light field control of electronic processes during laser-matter interactions. Thus, the measurement and control of CEP is essential for applications of few-cycle lasers. Currently, there is no robust method for measuring the non-trivial spatial CEP distribution of few-cycle laser pulses. Here, we demonstrate a compact on-chip, ambient-air, CEP scanning probe with $0.1 \mu\text{m}^3$ resolution based on optical driving of CEP-sensitive ultrafast currents in a metal–dielectric heterostructure. We successfully apply the probe to obtain a 3D map of spatial changes of CEP in the vicinity of an oscillator beam focus with pulses as weak as 1 nJ. We also demonstrate CEP control in the focal volume with a spatial light modulator so that arbitrary spatial CEP sculpting could be realized.

The evolution of the electric field of ultrashort laser pulses plays a crucial role in the dynamics of laser-matter interactions. Contemporary laser technology allows for straightforward control of the field shape through a property called the carrier-envelope phase (CEP), which describes the phase of the carrier wave with respect to the intensity envelope of a laser pulse. Robust techniques such as f-to-2f interferometry^{1–4} and above-threshold ionization stereometry⁵ enable laser users to CEP-stabilize laser pulse trains^{2,3} or measure CEP in phase tagging experiments^{6–9}. This has paved the way for the observation of many intriguing light-phase dependent phenomena related to photoionization of atoms^{10,11} and molecules,^{11,12} photoemission from metals^{13,14} and metallic nanoparticles,^{15,16} high-harmonic generation^{17,18}, photochemical reaction directional control^{19,20}, and optically induced current^{21–23}. At the same time, the ability to directly access the evolution of the electric field shape through CEP has been a key ingredient in attosecond science²⁴. However, as most experiments are conducted in the vicinity of the laser focus where the spatial distribution of CEP is non-trivial^{25,26}, demonstrations of CEP-sensitive interactions with larger structures, such as photoemission from arrays of nanoparticles^{15,27–29}, surface-enhanced Raman scattering on adsorbed molecules³⁰, high-

harmonic generation from gases and especially solids^{31,32}, current in reconfigurable circuits³³, or petahertz networks^{23,34}, are still pending, as the scaling of such systems is limited due to volume smearing effects. Here, we present a method for measuring and controlling CEP spatial distributions that enable the establishment of areas of well-defined CEP volumes. This will allow for the study of CEP effects in larger systems, which could become promising cornerstones for the development of attoscience-based real-life devices.

Some successful measurements of CEP spatial distributions have already been achieved by scanning a CEP-sensitive probe within the focal volume of a laser beam. One approach exploits the CEP sensitivity of a bunch of electrons emitted from a nanotip in vacuum²⁵. Another approach based on interferometry³⁵ relies on a superposition of sample and reference beams as a function of their respective delay. However, these methods have not found much utilization due to limitations, such as the need for a vacuum apparatus (nanotip method) or an interferometric setup. This calls for the design and implementation of compact, and easy-to-operate CEP devices for single-beam, non-interferometric and real-time measurements.

¹Wigner Research Centre for Physics, 1121 Budapest, Hungary. ²ELI-ALPS Research Institute, 6728 Szeged, Hungary. ³Physics Department, Ludwig-Maximilians-Universität, 85748 Munich, Germany. ⁴Max Planck Institute of Quantum Optics, 85748 Garching, Germany. ⁵Institute of Applied Physics, Abbe Center of Photonics, 07745 Jena, Germany. ⁶Fraunhofer Institute for Applied Optics and Precision Engineering, 07745 Jena, Germany.

✉ e-mail: hanus.vaclav@wigner.hu; dombi.peter@wigner.hu

In recent years, several CEP-sensitive on-chip devices were demonstrated, which have the potential to serve as the basis of an ambient-air and non-interferometric probe thanks to their small size. One such device is based on nanotunneling of electrons from a nanoparticle over a nm-sized junction to an anode^{36,37}. An array of nanoparticles has already been proven as a viable option to detect the CEP of laser beams^{38,39}, but no spatial resolution was demonstrated. Another method is based on the generation of light-field-driven ultrafast currents in dielectrics or semiconductors^{22,40}. The nonlinear strong-field interaction between the laser and electrons in the medium

couple the valence and the conduction band, rendering the medium virtually conductive^{23,41} for the duration of the strong laser field. Placing metal electrodes in the vicinity of the interaction volume enables the detection of currents whose magnitude and direction are CEP-dependent. A solid-state CEP measurement device was proposed based on this phenomenon⁷.

Here, we exploit the capability of light-field-driven ultrafast currents in solids²³ to measure spatial changes of the CEP and we construct an on-chip, ambient-air, single-beam, and compact probe with sub-micron resolution. Our new probe significantly differs from our earlier design published in ref. 23 so that a CEP change scanner device can be constructed. We implemented tapered electrodes, see Fig. 1a, b, on a thin metal–dielectric heterostructure of Ir and Al₂O₃ made by atomic-layer deposition (ALD) on a fused silica substrate⁴². The heterostructure has a nanolaminate structure and possesses a high $\chi^{(3)}$ that enhances the magnitude of CEP-sensitive currents, as already indicated in refs. 23,43. (Note that the electrodes are far enough from each other so that no electron tunneling can take place between them unlike in ref. 44). This way, we are able to characterize CEP distributions of focused laser beams formed by pulses having energy as low as 1 nJ. In combination with either spectral phase shaping or wavefront shaping using a spatial light modulator (SLM, Hamamatsu X15213-07), we measured and controlled CEP distributions in the vicinity of the laser beam focus.

Results

On-chip, ambient-air CEP probe

The design of the microscopic, ambient-air scanning CEP probe needs to satisfy two aspects: first, the active volume that is sensitive to the CEP needs to be small enough to allow resolution of the laser beam; second, the proportionality of the acquired phase being a function of CEP needs to be constant over a large range of intensities. The former was achieved by making lithographic gold electrodes in a shape of two opposing tapers and we estimate the volume resolution of our probe to be 0.1 μm^3 and a lateral resolution of 0.6 μm (determined by the electrode distance), see Fig. 1b and “Methods” for details on geometry. When illuminated with a laser beam phase-locked to a nonzero f_{CEO} frequency (1 kHz), our on-chip CEP probe generates an alternating current, whose amplitude J_0 and phase ϕ_J can be measured with a lock-in amplifier referenced to f_{CEO} . The current is steady exhibiting only 3.5° of standard deviation in ϕ_J in the time interval of 1 min, see Fig. 2d.

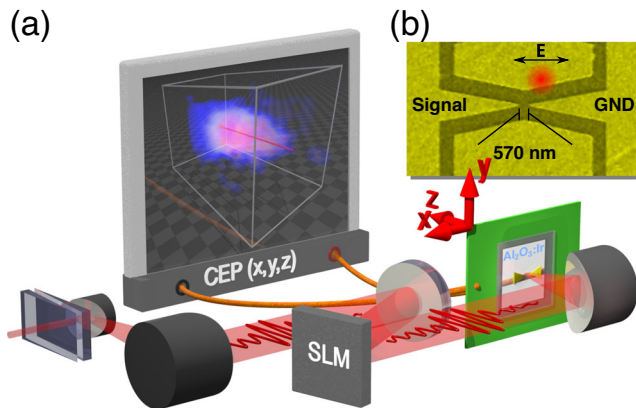


Fig. 1 | Scheme of the experimental setup. **a** The laser beam propagates through dispersion-control wedges and bounces off mirrors and the SLM. The focus of the beam after the parabolic mirror is scanned by XYZ positioning of the phase-scanner probe in the focal volume and the CEP(x,y,z) function is acquired (see 3D colour map as a cloud on the screen). The probe is connected via a transimpedance amplifier and a lock-in amplifier, so that the current J_0 and its phase ϕ_J could be measured at a reference frequency f_{CEO} . ϕ_J is then a direct measure of the CEP. **b** The SEM image of the design of the microscopic probe: Two gold electrodes denoted as *Signal* and *GND* shaped to a tapered ending are separated from each other by a ~ 570 nm gap. The red circle illustrates the impinging laser beam, and it is depicted in-scale with respect to the SEM image (the edge of the circle is at e^{-2} of the typical intensity profile). The black arrow depicts the direction of the laser polarization.

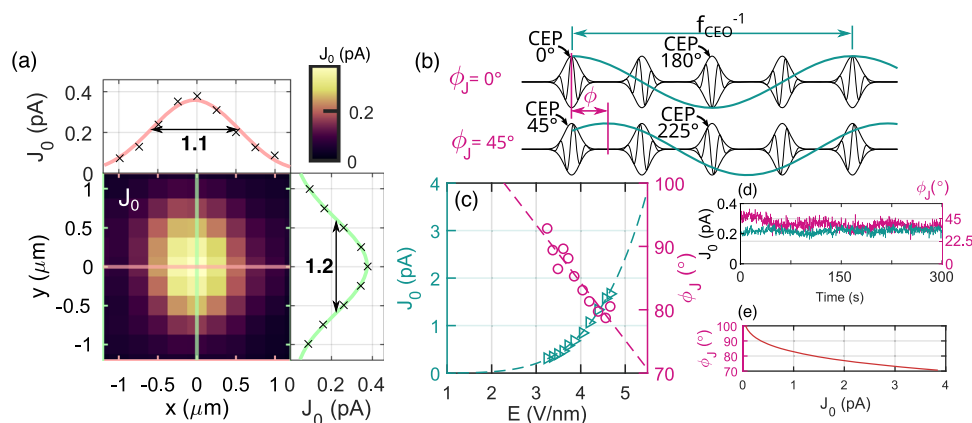


Fig. 2 | Current and phase response of the on-chip probe. **a** The heatmap shows a typical current magnitude J_0 profile resulting from an xy position scan in the laser polarization plane at the depth where the intensity is the highest. Side plots show cut-outs through the J_0 distribution vertically (green) and horizontally (pink) with respective Gaussian fits and the $1/\sqrt{e}$ diameter. **b** Illustration of measured lock-in phase ϕ_J and CEP equivalence. The two depicted pulse trains differ in CEP offset by 45°. This projects to the offset of the current oscillation in the connected circuit (green line) leading to the change in the detected lock-in phase ϕ_J by 45°.

c Measured lock-in current magnitude J_0 (green triangles) and phase ϕ_J (pink circles) as they are generated during the illumination of the CEP probe. The CEP probe and beam are kept stationary, while the power of the beam is changed resulting in the change of the electric field amplitude E . Dashed lines represent power law and linear fits, respectively. **d** Temporal stability of the current J_0 (green) and the phase ϕ_J (pink) from the probe tested for $t = 300$ s with 3 Hz acquisition rate. **e** The relationship between the fits of the measured current and the phase $\phi_J(J_0)$ which is used as a correction to the measured CEP scans.

As concluded in our previous work²³, φ_j follows the relative CEP offset of the laser pulse train. Hence, we label the measured phase φ_j as ΔCEP in the following figures. For better understanding of the validity of this equivalence, we provide an illustration in Fig. 2b, where two pulse trains on the picture represent two different spatial points with respective CEP offset of 45° . Consequently, the measured φ_j difference between these two points will be 45° as well. It turns out that φ_j has a slight dependence on the laser electric field: 7.5°nm/V , see Fig. 2c. We compensated for this property by introducing an empirical J_0 dependent offset $\varphi_j(J_0)$, see Fig. 2e and Supplementary information for details.

In order to demonstrate the sensitivity of our nJ-level CEP probe, we investigated a focus of a 2.5 nJ broad-spectrum oscillator laser beam providing pulses with $\tau = 5.5$ fs duration (intensity full-width at half-maximum, FWHM) at a repetition rate of 80 MHz, see Fig. 1a for a sketch of the setup. Due to losses in the beamline the typical pulse energy during the experiment was about 1.5 nJ. After a tight focusing (see “Methods”) we expect a peak intensity of up to 13×10^{12} W/cm², i.e., 7 V/nm field strength, and we obtain a CEP-sensitive current without any optical damage to the probe (note, that the CEP-dependent current should be observable already from 0.6 V/nm as indicated in ref. 23). A scan of J_0 with 250-nm-long steps in the polarization plane in the focal position (defined as a point on the optical axis where J_0 is the highest) reveals the resolution and range of the CEP probe in the polarization plane, see Fig. 2a. A measurable signal was acquired in the range $(-1.0w_0, +1.0w_0)$, $w_0 = 1.5$ μm , with a useful scanned area of 6.9 μm^2 . Note that the polarization is linear, and the electric field vector is parallel to the line connecting the two opposing electrodes. If the polarization is set perpendicular, the current drops almost to zero, see Supplementary information.

Oscillator beam spatial CEP distribution

The spatial $\Delta\text{CEP}(x, y, z)$ distribution of a short, broad-spectrum beam can acquire various shapes as measured in earlier studies^{25,26,35}, and supported by theoretical studies^{26,45–47}. In Fig. 3, we show a complete volumetric characterization of the CEP distribution around the laser beam focus ($w_0 = 1.7$ μm) as we scanned a useful volume of 84 μm^3 . Here, we use the following convention for the spatial coordinates: x –horizontal (laser polarization direction), y –vertical, z –optical axis, see Fig. 1a. To visualize the measurement, we have cut the measured 3D distribution into three slices intersecting at the point of highest current J_0 which is assumed to be the focus of the beam. We can see that in the laser focal plane, see Fig. 3c, which is also a plane of the highest laser intensity, the ΔCEP is not constant and tends to decrease in value outwards. In planes along the optical axis, see Fig. 3a, d, the CEP forms a ridge along the optical axis z , and the phase drops along z . The drop of CEP is asymmetric with respect to the point of highest J_0 ($z = 0$ μm) and ranges from 30° to -80° (extracted in Fig. 3c). This contrasts to a purely Gouy phase shift, which shows a symmetric drop of the CEP value.

To explain our observations, we need to consider chromatic aberrations that have a crucial influence on the CEP distribution^{45,46}. These aberrations can be approximated by introducing parameters g , γ , and C_r (chirp), which correspond to the first derivatives with respect to the frequency evaluated at the central frequency of: beam waist, focal position, and spectral phase, respectively, see “Methods” for their definition. The assumption of a Gaussian beam TEM₀₀ leads to an analytical model derived in ref. 45 and reproduced in Methods, Eq. (2). We compared the measurement with the model evaluated for certain g , γ , and C_r values. We found the best agreement for values: $g = 0.2$, $\gamma = 0.3$ and $C_r = -0.8$, see Fig. 3b, e, f. Despite performing the scan at a pulse compression setting where the CEP-sensitive signal J_0 reached its peak and maximum pulse compression was expected, it is noteworthy that a negative chirp value in the model was still necessary to match the measurements. This discrepancy can be explained by the negative

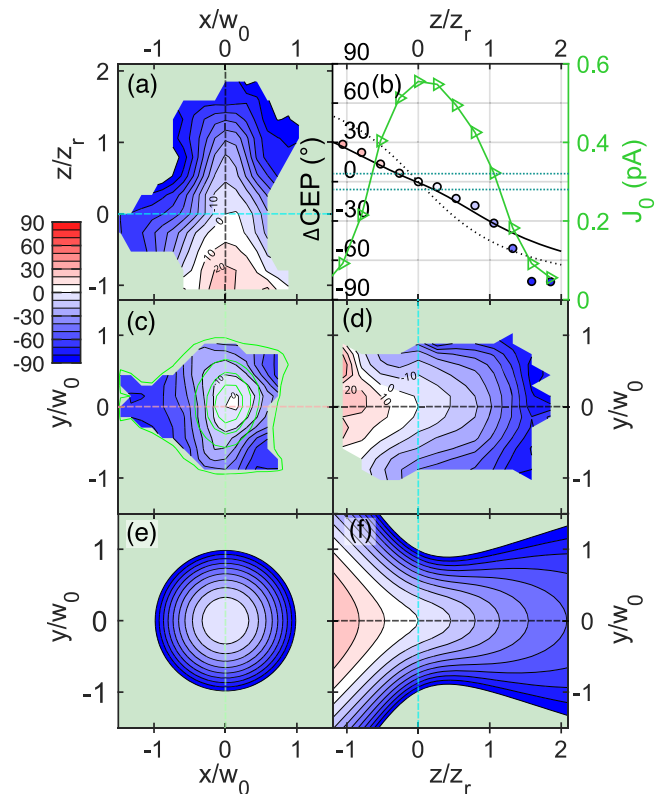


Fig. 3 | Spatial CEP distribution measured with the on-chip probe. a, c, d Cross-sections through the measured spatial change of CEP in degrees in the xz (horizontal), xy (transversal), yz (vertical) planes, where x and y are the axes along (horizontal) and perpendicular (vertical) to the laser polarization, respectively, and z is the laser beam propagation axis. The beam waist and the Rayleigh length of the measured beam are $w_0 = 1.7$ μm and $z_r = 11.3$ μm , respectively, with a central wavelength of 800 nm. **c** The phase map is overlapped with green contours of the measured current J_0 . Cuts go through the point of the highest J_0 . Dashed lines show the intersects of the plotted cuts: cyan for transversal, pink for horizontal and green for vertical. Phase and J_0 along the optical axis (black dashed line) are shown in **(b)**. Triangles and circles are the measured datapoints of the current amplitude J_0 and the CEP, respectively. The maximum of J_0 (green) signifies the position of the focus, where the measured phase was offset to zero. Solid black line shows the best fit of the model from Eq. (12) in ref. 45 with parameters $g = 0.2$, $\gamma = 0.3$, and $C_r = -0.8$. Dotted line is the $-\text{atan}(\frac{z}{z_r})$ function, i.e., Gouy phase. Dotted horizontal lines define the range of CEP used for the calculation of volume of flat phase being 9.6 μm^3 . **e, f** Show the model in xy (transversal), yz (vertical) plane.

curvature of the spectral phase at the central frequency, as indicated by the spectral phase reconstruction based on the dscan measurement. The negative value of C_r , corresponding to this negative chirp, can be attributed to the inherent challenge of achieving an ideally flat spectral phase for an octave-spanning laser pulse. Additional details can be found in the Supplementary information.

Arbitrary CEP control in the focal volume

One viable scheme to shaping of CEP landscape is the spectral phase manipulation accessible via pulse chirping⁴⁵. The theoretical investigations suggest that the presence of a non-flat spectral phase can lead to a significant bending of the phase profile in both axial and transversal direction. Indeed, the ridge structure presented in Fig. 3a, c, d was reproduced with a negative C_r value in the model (Fig. 3e, f). To illustrate the capabilities of the chirp to control the $\Delta\text{CEP}(x, y, z)$, we performed a measurement of CEP landscape for two positions of dispersion compensation wedges. The first settings, denoted as $d = 0$ mm, produced maximum current, while the other setting was produced by adding 0.5 mm fused silica glass in the beamline, i.e., $d = 0.5$ mm. This

corresponds to adding 18 fs^2 of group delay dispersion to the spectral phase $\varphi(\omega)$ and relative chirp C_r change of 0.8. The range of chirping is limited as with more chirp the laser pulse becomes longer, and consequently the signal from the probe becomes weaker, due to an increasing symmetry of the electric field under the envelope of the pulse. Results are presented in Fig. 4. Looking at the measured CEP distribution in Fig. 4, we note remarkable spatial changes that resulted from the addition of positive group delay dispersion: First, in the axial CEP distribution we can see an increase of steepness of the phase in the prefocal region and decrease of steepness after the focus, see Fig. 4c. Second, more glass resulted in flattening of the ridge structure observable in the horizontal xz slice, compare Fig. 4a2, b2. Evaluation of the model with $C_r = -0.8$ and $C_r = 0.0$ (with parameters $g = 0.4$, $\gamma = 0.1$) captures well the qualitative change of shape between cases $d = 0 \text{ mm}$ and $d = 0.5 \text{ mm}$, see Fig. 4a3, b3. As a consequence of the ridge reduction the area of flat CEP (CEP in the interval $(0^\circ, 10^\circ)$) in the vicinity of the intensity maximum increased. This flattening is very well

visible on the transverse slices in polarization plane xy , compare Fig. 4a1, b1.

Another way toward CEP landscape shaping is to modify the chromatic aberrations of the laser beam, which can influence g and γ . This can be achieved with lenses⁴⁵, but it is not feasible with few-cycle pulses. Instead, we exploited the chromatic behavior of the liquid-crystal on a silicon spatial light modulator (SLM) placed before the final focusing element in our beamline, see Fig. 1a. The SLM device introduces a phase shift as a function of position in the near-field and this phase shift is frequency (wavelength)-dependent. If a curved pattern is set on the SLM, it imprints a curvature on wavefronts and, in turn, causes a weak lensing effect on the laser beam. The curvature is frequency dependent, and this way the size of the beam $W_0(\omega)$ on the final focusing parabola is changed. Consequently, focal waists $w_0(\omega)$ and positions of foci $f(\omega)$ change, which are linked to g and γ . This can be particularly useful for laser beams produced by hollow-core fiber compressors that can carry a certain amount of chromatic aberration⁴⁸. The frequency dependent wavefront curvature induced by an SLM can be enough to invert the dependence of wavefront curvatures on wavelength, see the Supplementary information, for a discussion on SLM limitations.

To test the ΔCEP landscape manipulation with SLM, we applied the following curved pattern on the SLM as depicted in the inset of Fig. 5b. From the 3D scan of the focal volume with the CEP probe, we can see that the ΔCEP landscape indeed changed, as evidenced by a

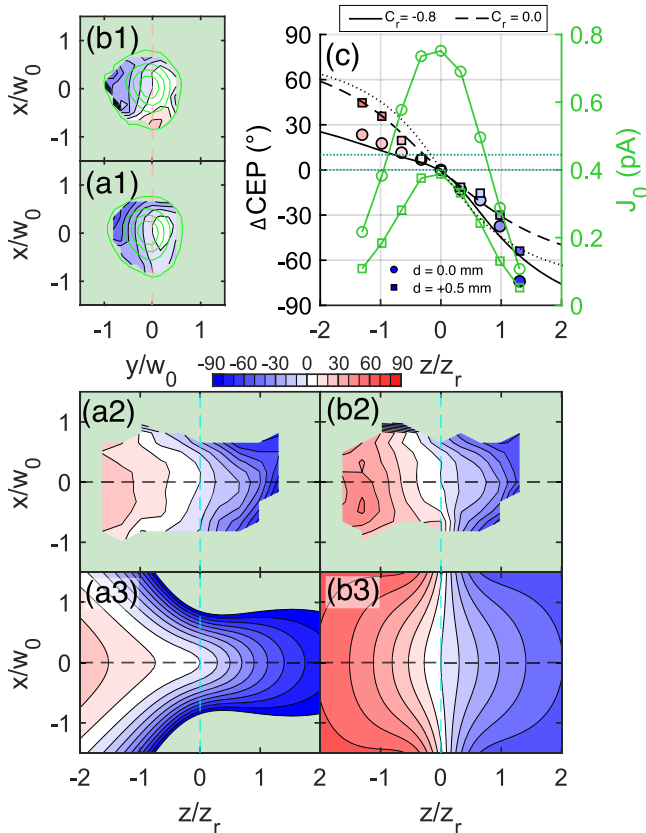


Fig. 4 | Effect of pulse chirp on the CEP landscape. Measured spatial change of the CEP in degrees in xz plane, where x, y are in-polarization horizontal and vertical axis, respectively, and z is the laser beam propagation axis. The beam waist and the Rayleigh length of the measured beam was $w_0 = 1.5 \mu\text{m}$ and $z_r = 8.8 \mu\text{m}$, respectively, with a central wavelength of 800 nm . Phase maps (a1, a2) were acquired for a pulse compression setting that provided the highest J_0 current, case denoted as $d = 0.0 \text{ mm}$. Phase maps (b1, b2) were acquired for a pulse compression created from (a) by adding 0.5 mm fused silica in the beamline, this case is denoted as $d = 0.5 \text{ mm}$. a3, b3 show the model, evaluated for parameters $C_r = -0.8$ and 0.0 , respectively. Other parameters in the model are the same and acquire values: $g = 0.4$, $\gamma = 0.1$. c We show the phase along the optical axis, which is highlighted in (a2) and (b2) as a black dashed line—circles: $d = 0.0 \text{ mm}$ and squares: $d = 0.5 \text{ mm}$ case. We accompany the datapoints with modeled phase values evaluated for chirp $C_r = -0.8$ and 0.0 , in solid and dashed line, respectively. The dotted line is the Gouy phase for a reference. Green lines are the J_0 current profiles of $d = 0.0 \text{ mm}$ (circles) and $d = 0.5 \text{ mm}$ (squares) case. The solid line is at the same time a lineout of the calculated CEP map in (a3) and (b3). Dotted horizontal lines in (c) define the range of CEP used for the calculation of the volume of flat phase.

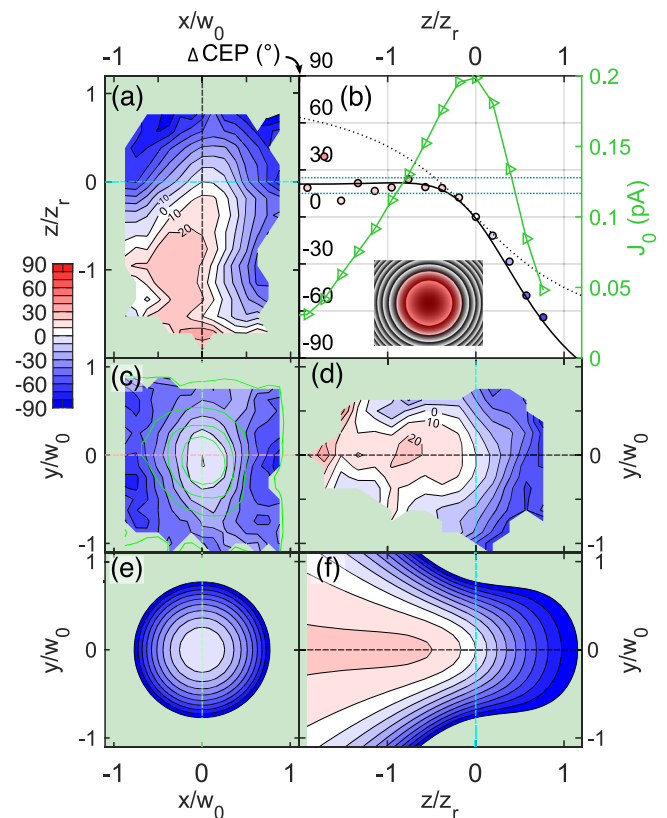


Fig. 5 | Exploiting chromatic aberrations to flatten the CEP. CEP phase flattening resulting from the beam shaping by the introduction of a chromatic aberration. Same representations as in Fig. 3. The beam waist and the Rayleigh length of the measured beam are $w_0 = 2.0 \mu\text{m}$ and $z_r = 15.7 \mu\text{m}$, respectively. The measured CEP map shows clearly a phase flattening in the prefocal region (a–d). The lineout along the black dashed line is shown in (b) with circles. Model in (e, f) and represented with the solid line in (b) is evaluated for values $g = 0.4$, $\gamma = -0.4$ and $C_r = -0.8$. Inset in (b) shows the applied SLM pattern with a red spot illustrating the beam size for scale. Dotted blue horizontal lines define the range of CEP used for the calculation of the volume of flat phase yielding $18.4 \mu\text{m}^3$.

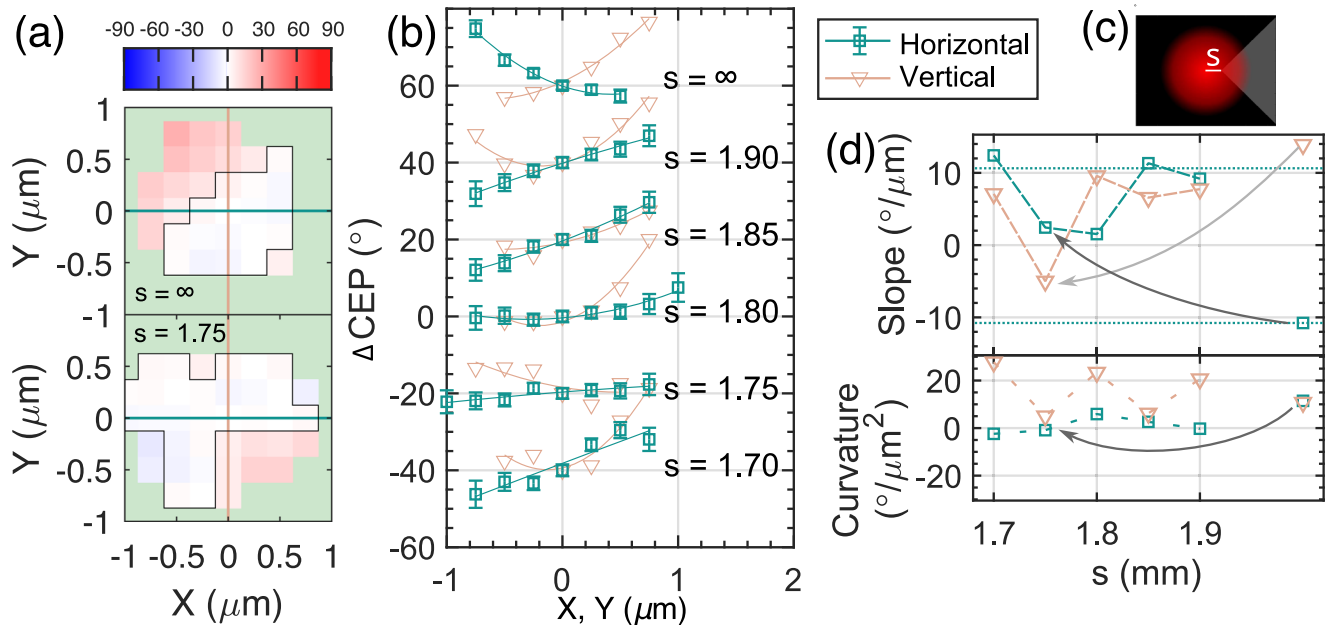


Fig. 6 | Controlling the slope of the CEP in the polarization plane. **a** Measured CEP change distribution in degrees in the plane perpendicular to the optical axis for two selected settings of SLM: $s = \infty$ (top) and $s = 1.75$ mm (bottom). The latter case illustrates how the application of SLM pattern improved the flatness of the phase along the horizontal (green line) direction. Light-green mask shades a region where signal is too low and phase measurement is obscured. Origin of the coordinate system is set to the point of largest J_0 . Black contour encircles the region where the CEP value is in the interval $(-5^\circ, +5^\circ)$. **b** CEP along horizontal (green squares) and vertical (beige triangles) slice as indicated in **(a)** for a range of values s . CEP is offset

by 20° for every s for the sake of legibility. Measured points are accompanied by polynomial fits. The length of error bars is proportional to J_0^{-1} . **c** Pattern applied on SLM with representation of parameter s . The red spot represents the size of beam used in the experiment in-scale. **d** Slope and curvature of the phase profiles from **(b)** obtained from fits for range of values s from an interval (1.7, 1.9) mm. The rightmost point is the case with zero SLM pattern. Arrows highlight the improvement in the slope and curvature when switching from zero pattern to SLM pattern with $s = 1.75$ mm.

comparison of Fig. 3a, c, d with Fig. 5a, c, d. Strikingly, we identify CEP flattening effect in the prefocal region, as the axial phase keeps steady at average value of $20 \pm 5^\circ$ in the axial range $(-1.7z_r, -0.3z_r)$, $z_r = 15.7 \mu\text{m}$. This feature is followed by a significant drop in phase value from 0° to -60° in $(0.0z_r, 1.4z_r)$. In the prefocal region, the flattening also extends in the lateral direction, see Fig. 5a, d, leading to a continuous and convex volume of $18.4 \mu\text{m}^3$ of flat phase settled between values $(15^\circ, 25^\circ)$. This is a significant improvement of the volume of approximately constant CEP compared to the case without the wavefront manipulation: The flat phase volume of the case presented in Fig. 3 yields only $9.6 \mu\text{m}^3$ of phase settled between values $(-5^\circ, 5^\circ)$. Furthermore, we have compared results of modified beam with a model. Its evaluation with parameters: $g = 0.4$, $\gamma = -0.4$, $C_r = -0.8$ gives a good agreement with the measurement, see Fig. 5b, e, f. We note the drop of γ by 0.7 in comparison with the measurement presented in Fig. 3 where the SLM was set to zero. This is well in agreement with the expectation that the chromatic properties defined by the size $W_0(\omega)$ of the beam on the final focusing parabola changed due to the use of the SLM.

In order to demonstrate the ΔCEP distribution sculpting using an SLM, our objective was to achieve a controlled change in the slope of the ΔCEP along the horizontal x axis. A trial calculation of a Fresnel integral showed that it is possible to achieve a horizontal tilt of the focal phase. This can be accomplished by applying a phase offset of π on the wavefront of the pupil electric field in two distinct regions, which are separated by a V-shaped border, see Fig. 6c and “Methods” for the discussion on the relation between the pupil function and CEP. To test this pattern, we first measured the distribution of ΔCEP in the plane perpendicular to the laser propagation direction when no SLM pattern was applied, this case is denoted as $s = \infty$. In Fig. 6a top, we show the ΔCEP in a point along the optical axis z where J_0 was the highest. From this data we plot the ΔCEP along the horizontal and

vertical directions through that point, see Fig. 6b. Finally, we applied a polynomial fit to acquire a measure of the slope and the curvature of the ΔCEP profile, see Fig. 6d. One can see that using a beam as is (without the SLM manipulation), we did not get a flat CEP response (see Fig. 6a top profile, and Fig. 6b topmost curve for $s = \infty$ case). Then the predefined SLM pattern was applied, and an xy -scan was performed in the same z position as in the case without the pattern. We varied the only free parameter s , which represents the distance of the V-shape apex from the center of the SLM chip in millimeters. We can see in Fig. 6b that the horizontal CEP profile indeed changes with changing the SLM pattern, while the optimal setting was found for $s = 1.75$. The exclusivity of this point for our setup is confirmed also with the low value of the slope and curvature obtained from the fits. In addition, we show the full CEP profile in the scanned xy -plane for this s value in Fig. 6a bottom. Apart from flattening the phase along a line, the area of constant phase, defined as an area where the phase is the interval between $(-5^\circ, +5^\circ)$ increased from 1.06 to $1.63 \mu\text{m}^2$ by applying the optimal SLM pattern. Our experiment thus shows that it is possible to use a feedback loop to gain control over the CEP landscape.

Discussion

We demonstrated a compact, on-chip, and single-beam CEP scanner device operating under ambient laboratory conditions. The technique relies on the generation of CEP-sensitive ultrafast currents in a thin nanolaminate coating. The currents are detected using a microscopic electric probe with a sensitive volume of $0.1 \mu\text{m}^3$. The probe is assembled on an optical chip. We anticipate that our technique is compatible with a wide range of laser systems providing laser pulse energy > 1 nJ as long as the measured laser pulse is of few-cycle character and they are phase-locked to a nonzero f_{CEO} . The applicability to systems that lock to $f_{\text{CEO}} = 0$ can be ensured by, for example, introducing a piezo-driven mechanical CEP modulation with wedges.

We also showed that the use of an SLM is a viable option to sculpt the CEP distribution of a laser beam. We demonstrated a control of the spatial change of the CEP, including CEP flattening in the focal volume. We propose that the CEP probe could be a part of a feedback mechanism that would ultimately enable arbitrary CEP sculpting. We foresee that CEP scans will pave the way towards observations of new phenomena that were previously hindered by volume CEP smearing and would otherwise have to rely on the signal from small volumes.

Methods

Active material and electrode design

For the CEP-probe fabrication we utilized a 1D-nanolaminate-coated slab on top of which we patterned gold electrodes using electron beam lithography. The nanolaminate heterostructure consists of alternating atomically thin layers of Al₂O₃ and Ir metal⁴⁹ and was prepared using atomic-layer deposition (see the Supplementary information for fabrication details). We showed that the presence of the nanolaminate increases the detected current in the probe compared to a bare dielectric medium, see the Supplementary information for this comparison. The coating itself limits the depth of the active volume that generates the ultrafast currents to its thickness, which was 227 nm. Next, the lateral size of the active volume is limited by the shape of the electrodes. The horizontal size (laser polarization direction) is bounded by the distance between the electrodes which was designed to be 570 nm. The vertical size (perpendicular to laser polarization) is defined by the width of the electrodes. To push this resolution to the maximum we opted for a triangular shape of the electrodes with a sharp vertex, so that the vertical dimension of the active volume is shorter than the horizontal one, see Fig. 1b. Overall, taking the upper limit for the vertical size same as the distance between electrodes: 570 nm, we end up with an active volume, i.e., volumetric resolution of 0.1 μm³.

Acquisition method

The CEP probe was moved in steps of 3 or 5 μm along the optical axis and 250 nm in the polarization plane. As the CEP probe is being moved step-by-step in the beam being tested, we acquire the magnitude of the current J_0 at phase φ_j as a function of spatial coordinates x , y , and z . The speed of the CEP scan was limited by the speed of the moving stage and the relationship between the bandwidth of the preamplifier and f_{CEO} . In this work, the preamplifier's (FEMTO® Messtechnik GmbH, DLPCA-200) bandwidth was 1 kHz, f_{CEO} was 1 kHz and 30 ms settling time (time constant) of the lock-in amplifier, which could theoretically allow detection speeds up to 30 samples/s. In the measurements presented here, the limit was the moving stage as its motion speed was about 2 Hz. If the f_{CEO} was higher and the motion speed would be improved one could achieve an effective real-time feedback loop.

Laser beam focusing

To reach the required on-target intensity the beam was expanded by a reflective off-axis parabola telescope to 6 mm FWHM in the intensity and then focused with an off-axis parabola of 15 mm focal length. This gives a theoretical low limit for the waist of the focus of 0.75 μm (intensity FWHM). Due to the wide spectrum and aberrations introduced by the use of parabolic mirrors in the beamline, the achievable size of the focal spot in terms of waist w_0 was below 1.7 μm. The size was determined with a knife-edge method, see the Supplementary information.

Theoretical range of scanning

The amount of maximum intensity available will determine the size of volume that can be scanned. However, an estimate can be done in terms of length normalized to beam parameters w_0 and z_r , being beam waist and Rayleigh length, respectively. In the best-case scenario, assuming conditions of our experiment and a Gaussian spatial profile

of the beam, we can expect CEP sensitivity of the probe up to radius $1.6w_0$ in the laser focal plane. Concerning the sensitivity range along the laser propagation axis, we can expect a theoretical threshold of the on-axis CEP signal up to $12z_r$.

Definition of g , γ , and C_r

The analytical model used in this work uses parameters g and γ to describe the chromatic aberrations of the spectrally broad laser beam:

$$g = 1 + \frac{2w'_0}{w_0} \omega_0, \gamma = \frac{f'}{z_r} \omega_0 \quad (1)$$

where w_0 is the beam waist, f is the focal position, z_r is the Rayleigh length, and the prime sign stands for a derivative with respect to frequency ω evaluated at the central frequency, which is in our case $\omega_0 = 2.356$ rad/fs. In addition, the $\Delta\text{CEP}(x,y,z)$ is also a function of the spectral phase, i.e., in the first approximation chirp. Throughout this work we use a relative chirp defined as $C_r = 2\ln(2)C/r^2$, where C is the chirp. For a pulse with a spectrum $E(\omega) = \sqrt{S(\omega)} \exp(-i\varphi(\omega))$, $C = 2\varphi''(\omega_0)$, i.e., the chirp is equivalent to the group velocity dispersion and can be estimated from the second derivative of spectral phase at the central frequency.

Model for calculating CEP spatial maps

To model the $\Delta\text{CEP}(x,y,z)$ spatial map, we used an analytical formula from⁴⁵:

$$\Delta\text{CEP}(r,z) = -\tan^{-1}\left(\frac{z}{z_r}\right) + \frac{1 - 2\frac{r^2}{w^2(z)}}{1 + \left(\frac{z}{z_r}\right)^2} \times \left[G\left(\frac{z}{z_r}\right) + \Gamma\left(\frac{z}{z_r}\right)^2 \right] + [\Gamma + 2C_r] \frac{r^2}{w^2(z)} \quad (2)$$

where

$$G = g - 2\gamma C_r, \Gamma = \gamma + 2g C_r \quad (3)$$

with a radial coordinate $r^2 = x^2 + y^2$ and z being the distance along the optical axis. We use the Eq. (2) in Figs. 3–5 as well as for selected cases of C_r and g in the Supplementary information. The model clearly shows how the parameters g , γ or C_r (representing the first approximation of the spectral characteristic of the laser beam) can modify the CEP evolution in space.

Relation between pupil function and CEP

We showed that a shaping of the phase front of the pupil function with SLM can affect the CEP landscape. We would like to comment on the relationship between the pupil function and the CEP distributions around the laser focus. Although the SLM does not affect the CEP directly, it adds phase to the laser beam wavefronts which in turn is added to the focal phase distribution. Mathematically speaking, the distribution of the electric field in the focal plane is a Fresnel integral over the pupil function. Thus, shaping the pupil function has the potential to change the intensity and phase distribution about the focal plane. Clearly, the CEP phase is not just the phase of the wavefront, but it results from its relation to the pulse-front surfaces. Therefore, the complete relationship between the pupil function and the focal CEP phase requires demanding spatiotemporal modeling that is beyond the scope of this paper. Here, we decided to overcome this complexity and for the sake of proof-of-principle experiments, we do not aspire to prove the relationship between the pupil function and the focal CEP phase, but we intend to show that it is possible to realize a feedback loop where step-by-step optimization of a pupil function leads to a desired CEP phase distribution in the focus.

Data availability

The data that support the findings of this study are available from the corresponding author upon request.

References

1. Telle, H. R. et al. Carrier-envelope offset phase control: a novel concept for absolute optical frequency measurement and ultrashort pulse generation. *Appl. Phys. B* **69**, 327–332 (1999).
2. Apolonski, A. et al. Controlling the phase evolution of few-cycle light pulses. *Phys. Rev. Lett.* **85**, 740–743 (2000).
3. Jones, D. J. et al. Carrier-envelope phase control of femtosecond mode-locked lasers and direct optical frequency synthesis. *Science* **288**, 635–639 (2000).
4. Reichert, J., Holzwarth, R., Udem, T. & Hänsch, T. W. Measuring the frequency of light with mode-locked lasers. *Opt. Commun.* **172**, 59–68 (1999).
5. Paulus, G. G. et al. Measurement of the phase of few-cycle laser pulses. *Phys. Rev. Lett.* **91**, 253004 (2003).
6. Saylor, A. M. et al. Precise, real-time, every-single-shot, carrier-envelope phase measurement of ultrashort laser pulses. *Opt. Lett.* **36**, 1–3 (2011).
7. Paasch-Colberg, T. et al. Solid-state light-phase detector. *Nat. Photonics* **8**, 214–218 (2014).
8. Kubullek, M. et al. Single-shot carrier-envelope-phase measurement in ambient air. *Optica* **7**, 35 (2020).
9. Rathje, T. et al. Review of attosecond resolved measurement and control via carrier-envelope phase tagging with above-threshold ionization. *J. Phys. B. Mol. Opt. Phys.* **45**, 074003 (2012).
10. Paulus, G. G. et al. Absolute-phase phenomena in photoionization with few-cycle laser pulses. *Nature* **414**, 182–184 (2001).
11. Liu, X. et al. Nonsequential double ionization at the single-optical-cycle limit. *Phys. Rev. Lett.* **93**, 1–4 (2004).
12. Hanus, V. et al. Experimental separation of subcycle ionization bursts in strong-field double ionization of H₂. *Phys. Rev. Lett.* **124**, 103201 (2020).
13. Apolonski, A. et al. Observation of light-phase-sensitive photoemission from a metal. *Phys. Rev. Lett.* **92**, 1–4 (2004).
14. Dombi, P. et al. Direct measurement and analysis of the carrier-envelope phase in light pulses approaching the single-cycle regime. *N. J. Phys.* **6**, 39 (2004).
15. Piglosiewicz, B. et al. Carrier-envelope phase effects on the strong-field photoemission of electrons from metallic nanostructures. *Nat. Photonics* **8**, 37–42 (2014).
16. Földi, P., Márton, I., Németh, N., Ayadi, V. & Dombi, P. Few-cycle plasmon oscillations controlling photoemission from metal nanoparticles. *Appl. Phys. Lett.* **106**, 013111 (2015).
17. Ishii, N. et al. Carrier-envelope phase-dependent high harmonic generation in the water window using few-cycle infrared pulses. *Nat. Commun.* **5**, 1–6 (2014).
18. Baltuška, A. et al. Attosecond control of electronic processes by intense light fields. *Nature* **421**, 611–615 (2003).
19. Kübel, M. et al. Steering proton migration in hydrocarbons using intense few-cycle laser fields. *Phys. Rev. Lett.* **116**, 1–6 (2016).
20. Alnaser, A. S. & Litvinyuk, I. V. Subfemtosecond directional control of chemical processes in molecules. *J. Phys. B. Mol. Opt. Phys.* **50**, 032002 (2017).
21. Fortier, T. M. et al. Carrier-envelope phase-controlled quantum interference of injected photocurrents in semiconductors. *Phys. Rev. Lett.* **92**, 1–4 (2004).
22. Schiffrin, A. et al. Optical-field-induced current in dielectrics. *Nature* **493**, 70–74 (2013).
23. Hanus, V. et al. Light-field-driven current control in solids with pJ-level laser pulses at 80 MHz repetition rate. *Optica* **8**, 570 (2021).
24. Krausz, F. & Ivanov, M. Attosecond physics. *Rev. Mod. Phys.* **81**, 163–234 (2009).
25. Hoff, D. et al. Tracing the phase of focused broadband laser pulses. *Nat. Phys.* **13**, 947–951 (2017).
26. Hoff, D. et al. Using the focal phase to control attosecond processes. *J. Opt.* **19**, 124007 (2017).
27. Lovász, B. et al. Nonadiabatic nano-optical tunneling of photoelectrons in plasmonic near-fields. *Nano Lett.* **22**, 2303–2308 (2022).
28. Dombi, P. et al. Ultrafast strong-field photoemission from plasmonic nanoparticles. *Nano Lett.* **13**, 674–678 (2013).
29. Dombi, P. et al. Strong-field nano-optics. *Rev. Mod. Phys.* **92**, 025003 (2020).
30. Liu, J. & Li, Z. Control of surface plasmon resonance in silver nanocubes by CEP-locked laser pulse. *Photonics* **9**, 53 (2022).
31. Korobenko, A. et al. In-situ nanoscale focusing of extreme ultraviolet solid-state high harmonics. *Phys. Rev. X* **12**, 41036 (2022).
32. Vampa, G. et al. Plasmon-enhanced high-harmonic generation from silicon. *Nat. Phys.* **13**, 659–662 (2017).
33. Jana, K. et al. Reconfigurable electronic circuits for magnetic fields controlled by structured light. *Nat. Photonics* **15**, 622–626 (2021).
34. Boolakee, T. et al. Light-field control of real and virtual charge carriers. *Nature* **605**, 251–255 (2022).
35. Major, B., Nemes, D., Porras, M. A., Horváth, Z. L. & Kovács, A. P. Carrier-envelope phase changes in the focal region: propagation effects measured by spectral interferometry. *Appl. Opt.* **54**, 10717 (2015).
36. Rybka, T. et al. Sub-cycle optical phase control of nanotunnelling in the single-electron regime. *Nat. Photonics* **10**, 667–670 (2016).
37. Putnam, W. P., Hobbs, R. G., Keathley, P. D., Berggren, K. K. & Kärtner, F. X. Optical-field-controlled photoemission from plasmonic nanoparticles. *Nat. Phys.* **13**, 335–339 (2017).
38. Yang, Y. et al. Light phase detection with on-chip petahertz electronic networks. *Nat. Commun.* **11**, 3407 (2020).
39. Bionta, M. R. et al. On-chip sampling of optical fields with attosecond resolution. *Nat. Photonics* **15**, 456–460 (2021).
40. Paasch-Colberg, T. et al. Sub-cycle optical control of current in a semiconductor: from the multiphoton to the tunneling regime. *Optica* **3**, 1358 (2016).
41. Langer, F. et al. Few-cycle lightwave-driven currents in a semiconductor at high repetition rate. *Optica* **7**, 276 (2020).
42. Paul, P. et al. Atomically thin metal-dielectric heterostructures by atomic layer deposition. *ACS Appl. Mater. Interfaces* **15**, 22626–22636 (2023).
43. Khurgin, J. B. Optically induced currents in dielectrics and semiconductors as a nonlinear optical effect. *J. Opt. Soc. Am. B* **33**, C1 (2016).
44. Ludwig, M. et al. Sub-femtosecond electron transport in a nanoscale gap. *Nat. Phys.* **16**, 341–345 (2019).
45. Porras, M. A., Horváth, Z. L. & Major, B. Three-dimensional carrier-envelope-phase map of focused few-cycle pulsed Gaussian beams. *Phys. Rev. A* **98**, 063819 (2018).
46. Major, B., Horváth, Z. L. & Porras, M. A. Phase and group velocity of focused, pulsed Gaussian beams in the presence and absence of primary aberrations. *J. Opt.* **17**, 065612 (2015).
47. Porras, M. A. & Dombi, P. Freezing the carrier-envelope phase of few-cycle light pulses about a focus. *Opt. Express* **17**, 19424 (2009).
48. Alonso, B. et al. Characterization of sub-two-cycle pulses from a hollow-core fiber compressor in the spatiotemporal and spatio-spectral domains. *Appl. Phys. B Lasers Opt.* **112**, 105–114 (2013).
49. Schmitt, P. et al. Influence of substrate materials on nucleation and properties of iridium thin films grown by ALD. *Coatings* **11**, 173 (2021).

Acknowledgements

We acknowledge support from a FET Open Grant of the EU (PetaCOM 829153) and from the National Research, Development and Innovation

Office of Hungary (Projects 137373, TKP-2021-NVA-04 and 2018-1.2.1-NKP-2018-00012). We thank Balázs Major for discussions. The development of Ir/Al₂O₃ heterostructures was supported by the German Research Foundation (DFG, Deutsche Forschungsgemeinschaft) Collaborative Research Center (CRC/SFB) 1375 “NOA—Nonlinear Optics down to Atomic scales”—project B3, number 398816777, and the Fraunhofer Society Attract Project (grant number O66- 601020), Fraunhofer IOF Center of Excellence in Photonics.

Author contributions

V.H. and P.D. conceived and designed the experiments; V.H., B.F., and V.C. performed the experiments; V.H. and P.S. analyzed the data; Z.P., J.B., Z.W., P.P., and A.S. contributed with materials/analysis tools; V.H. and P.D. wrote the paper.

Funding

Open access funding provided by ELKH Wigner Research Centre for Physics.

Competing interests

The authors declare no competing interests.

Additional information

Supplementary information The online version contains supplementary material available at <https://doi.org/10.1038/s41467-023-40802-z>.

Correspondence and requests for materials should be addressed to Václav Hanus or Péter Dombi.

Peer review information *Nature Communications* thanks the anonymous, reviewer(s) for their contribution to the peer review of this work. A peer review file is available.

Reprints and permissions information is available at <http://www.nature.com/reprints>

Publisher's note Springer Nature remains neutral with regard to jurisdictional claims in published maps and institutional affiliations.

Open Access This article is licensed under a Creative Commons Attribution 4.0 International License, which permits use, sharing, adaptation, distribution and reproduction in any medium or format, as long as you give appropriate credit to the original author(s) and the source, provide a link to the Creative Commons licence, and indicate if changes were made. The images or other third party material in this article are included in the article's Creative Commons licence, unless indicated otherwise in a credit line to the material. If material is not included in the article's Creative Commons licence and your intended use is not permitted by statutory regulation or exceeds the permitted use, you will need to obtain permission directly from the copyright holder. To view a copy of this licence, visit <http://creativecommons.org/licenses/by/4.0/>.

© The Author(s) 2023